Multifunctional Materials: A Case Study of the Effects of Metal Doping on ZnO Tetrapods with Bismuth and Tin Oxides

Vasile Postica, Jorit Gröttrup, Rainer Adelung, Oleg Lupan,* Abhishek Kumar Mishra,* Nora H. de Leeuw, Nicolai Ababii, José F. C. Carreira, Joana Rodrigues, Nebiha Ben Sedrine, Maria Rosário Correia, Teresa Monteiro, Victor Sontea, and Yogendra Kumar Mishra**

Hybrid metal oxide nano- and microstructures exhibit novel properties, which make them promising candidates for a wide range of applications, including gas sensing. In this work, the characteristics of the hybrid ZnO-Bi_2O_3 and ZnO-Zn_2SnO_4 tetrapod (T) networks are investigated in detail. The gas sensing studies reveal improved performance of the hybrid networks compared to pure ZnO-T networks. For the ZnO-T-Bi_2O_3 networks, an enhancement in H_2 gas response is obtained, although the observed p-type sensing behavior is attributed to the formed junctions between the arms of ZnO-T covered with Bi_2O_3 and the modulation of the regions where holes accumulate under exposure to H_2 gas. In ZnO-T-Zn_2SnO_4 networks, a change in selectivity to CO gas with high response is noted. The devices based on individual ZnO-T-Bi_2O_3 and ZnO-T-Zn_2SnO_4 structures showed an enhanced H_2 gas response, which is explained on the basis of interactions (electronic sensitization) between the ZnO-T arm and Bi_2O_3 shell layer and single Schottky contact structure, respectively. Density functional theory-based calculations provide mechanistic insights into the interaction of H_2 and CO gas molecules with Bi- and Sn-doped ZnO(0001) surfaces, revealing changes in the Fermi energies, as well as charge transfer between the molecules and surface species, which facilitate gas sensing.

1. Introduction

Recent reports have demonstrated attractive sensing properties of single ZnO tetrapods (ZnO-T) or crossed zinc oxide nanorods.[1,2] However, despite the high sensitivity of individual structures, they commonly exhibit several disadvantages, including a slow response rate at room temperature and the need for expensive equipments.[1–6] The connection of ZnO-T into networks can be an effective way to increase the sensitivity and response rate through specific and improved sensing mechanisms considering an increased number of potential barriers between external connections.[7–12] Furthermore, due to the random alignments and the high aspect ratio of the ZnO-T nano- and microstructures, there is high probability for the formation of interconnections allowing continuous paths for current flow through the ZnO-T networks.[7]

V. Postica, Prof. O. Lupan, N. Ababii, Prof. V. Sontea
Department of Microelectronics and Biomedical Engineering
Technical University of Moldova
168 Stefan cel Mare Av., MD-2004 Chisinau, Republic of Moldova
E-mail: ollu@tf.uni-kiel.de, oleg.lupan@mib.utm.md

J. Gröttrup, Prof. R. Adelung, Prof. O. Lupan, Dr. Y. K. Mishra
Functional Nanomaterials
Institute for Materials Science
Kiel University
Kaiserstr. 2, D-24143 Kiel, Germany
E-mail: ra@tf.uni-kiel.de; ykm@tf.uni-kiel.de

Dr. A. K. Mishra
Research & Development, University of Petroleum and Energy Studies (UPES)
Bidholi, Dehradun 248007, India
E-mail: akmishra@ddn.upes.ac.in

Prof. N. H. de Leeuw
Department of Chemistry
University College London
20 Gordon Street, London WC1H 0AJ, UK

Prof. N. H. de Leeuw
School of Chemistry
Cardiff University
Main Building, Park Place, Cardiff CF10 3AT, UK

J. F. C. Carreira, Dr. J. Rodrigues, Dr. N. Ben Sedrine, Prof. M. R. Correia, Prof. T. Monteiro
Department of Physics and I3N
Institute for Nanostructures
Nanomodelling and Nanofabrication
University of Aveiro
3810-193 Aveiro, Portugal

The copyright line of this paper was changed 29 March 2017 after initial publication.

DOI: 10.1002/adfm.201604676

In the case of reducing gases for n-type nanostructures-based gas sensors, besides a high I_{gas}/I_{air} ratio and fast rise/decay times, one of the principal gas sensor characteristics is the selectivity to specific gases and also chemical species. Most of the conventional gas sensors based on ZnO and SnO_2 usually suffer from cross-sensitivity to other gases.[13] Thus, it is essential to develop a cost-effective method to fabricate highly selective sensors with an improved gas response over the normal ZnO and SnO_2. Controlling the crystallinity, crystal size and shape, effective surface area, and porosity are some of the principal parameters for tuning the selectivity and sensitivity of the gas sensors.[5,6,14–18] The doping of semiconducting oxides is another effective way to improve the gas sensing properties of devices, which results in tuning the concentration of charge carriers enabling the modulation of the Debye length[15,19] and is often referred to as "electronic sensitization." In turn, the doping effect promotes the creation of defects that can lead to an improvement of the gas sensing properties of the base-sensing material.[4,5,11,20] However, depending on the synthesis method, the high doping concentrations may contribute to the appearance of a dopant-related second phase and also to segregation effects on the surface of semiconducting oxide nanostructures.[21,22] Consequently, the micro- and nano-heterojunctions are formed, leading to interesting new sensing properties.[21,22]

Nano- and microscale ZnO tetrapods form a highly porous interconnected three-dimensional (3D) structure with a large surface-to-volume ratio having many gas diffusion channels, and are therefore excellent candidates for fabricating sensor devices with enhanced gas sensing response.[9,22] Sensors based on undoped ZnO-T networks with a high response to ethanol,[9,11,23] acetaldehyde,[24] and H_2S gas[10] have been reported. The formation of heterojunctions in these tetrapodal networks seems to be the main key and an efficient phonomenon to further improve the sensing properties of the ZnO-T.[25] Recently, novel hybrid materials based on highly porous ZnO-T 3D networks with different types of metal oxides (Me_xO_y) and ternary alloyed systems ($Zn_xMe_{1-x}O_y$), have been synthesized by a simple flame transport synthesis (FTS) approach.[22,26]

In this work, hybrid networks of ZnO-T with Zn_2SnO_4 and ZnO-T with Bi_2O_3 were synthesized by the FTS approach and their morphological, structural, vibrational, optical, chemical, and sensing properties were investigated in detail. In comparison with pure ZnO-T networks synthesized by the same procedure, the formation of additional microstructures on the surfaces of tetrapods were observed after the synthesis of ZnO-T in the presence of Sn-metal microparticles followed by thermal annealing. Subsequent characterization demonstrated that these additional microparticles consist of Zn_2SnO_4 in the crystalline phase. In the case of Bi-doped ZnO-T samples, ZnO and Bi_2O_3 crystalline phases were detected. Sensing measurements revealed improved properties for the detection of CO and H_2 gases, due to heterojunctions formed between the ZnO-T and the Zn_2SnO_4 and Bi_2O_3 hybrid systems. Furthermore, the devices based on individual hybrid structures of ZnO-T-Bi_2O_3 and ZnO-T-Zn_2SnO_4 with ultra-high H_2 gas response have been fabricated. Calculations based on density functional theory (DFT) have been carried out to model the Bi- and Sn-doped ZnO(0001) surfaces and their interaction with H_2 and CO gas molecules. The gas sensing behavior observed from the calculations is similar to the H_2 molecules interaction on doped CuO[14b] and ZnO[27] surfaces, where charge transfer and Fermi energy changes were found as indicators of the gas sensing mechanisms.

2. Results and Discussions

2.1. Morphological Studies of Hybrid 3D Networks (ZnO-T-Me_xO_y and ZnO-T-$Zn_xMe_{1-x}O_y$)

Scanning electron microscopy (SEM) images of ZnO-T-Bi_2O_3 hybrid networks (ZnO:Bi 20:1 and ZnO:Bi 10:1) are presented in **Figure 1**a,b and Figure 1c,d, respectively. It has been observed that the highly porous 3D networks are composed of dense interconnected ZnO-T nano- and microstructures with a size range of 20–100 µm (see Figure S1a, Supporting Information). Representative interconnections in the networks after annealing at 1150 °C for 5 h are presented in Figure S2 (Supporting Information). In comparison with pure ZnO-T networks,[8,22] the clear hexagonal shape of the tetrapod arms disappears after annealing the ZnO with Bi metal microparticles (Figures S1b–f and S2, Supporting Information). A layered structure at the end of the tetrapod arms can clearly be observed for ZnO-T-Bi_2O_3 hybrid 3D networks (Figure S1b–f, Supporting Information). Furthermore, for the highest concentration of Bi metal microparticles, the nanodots are formed on the surface of ZnO-T-Bi_2O_3 inteconnected samples (Figure S2, Supporting Information). The development of secondary microparticles, as is the case of hybrid networks with other types of metal oxides,[22] along with an essential change in the dimensions of ZnO-T, was absent for the synthesized hybrid ZnO-T-Bi_2O_3 samples.

In the hybrid 3D networks consisting of ZnO-T and Zn_2SnO_4 (ZnO:Sn 30:1, see Figure 1e,f and Figure S3a,b, Supporting Information), interconnected ZnO-T were formed with sizes in the range of 30–150 µm. Increasing the concentration of the Sn metal microparticles (ZnO:Sn 15:1, see Figure 1g,h), we observed the formation of microparticles randomly distributed through the network (Figure S3, Supporting Information). As observed previously for ZnO-T networks with other metal oxides,[22] the arising of a second type of spherical microparticles was promoted under the used synthesis conditions; an increase in the concentration of Sn metal microparticles results in larger agglomerates and a denser distribution of the additional spherical Zn_2SnO_4 microparticles.[22] In both cases, that is, ZnO-T-Bi_2O_3 and ZnO-T-Zn_2SnO_4 hybrid networks, the changes in morphology by increasing the content of metal particles is difficult to observe due to the large range of tetrapods dimensions. However, the essential changes were not observed by SEM in both cases.

2.2. Chemical and Structural Study of Hybrid 3D Networks

Elemental mappings, at high and low magnifications, of the ZnO-T and ZnO-T-Bi_2O_3 hybrid networks (ZnO:Bi 20:1) are

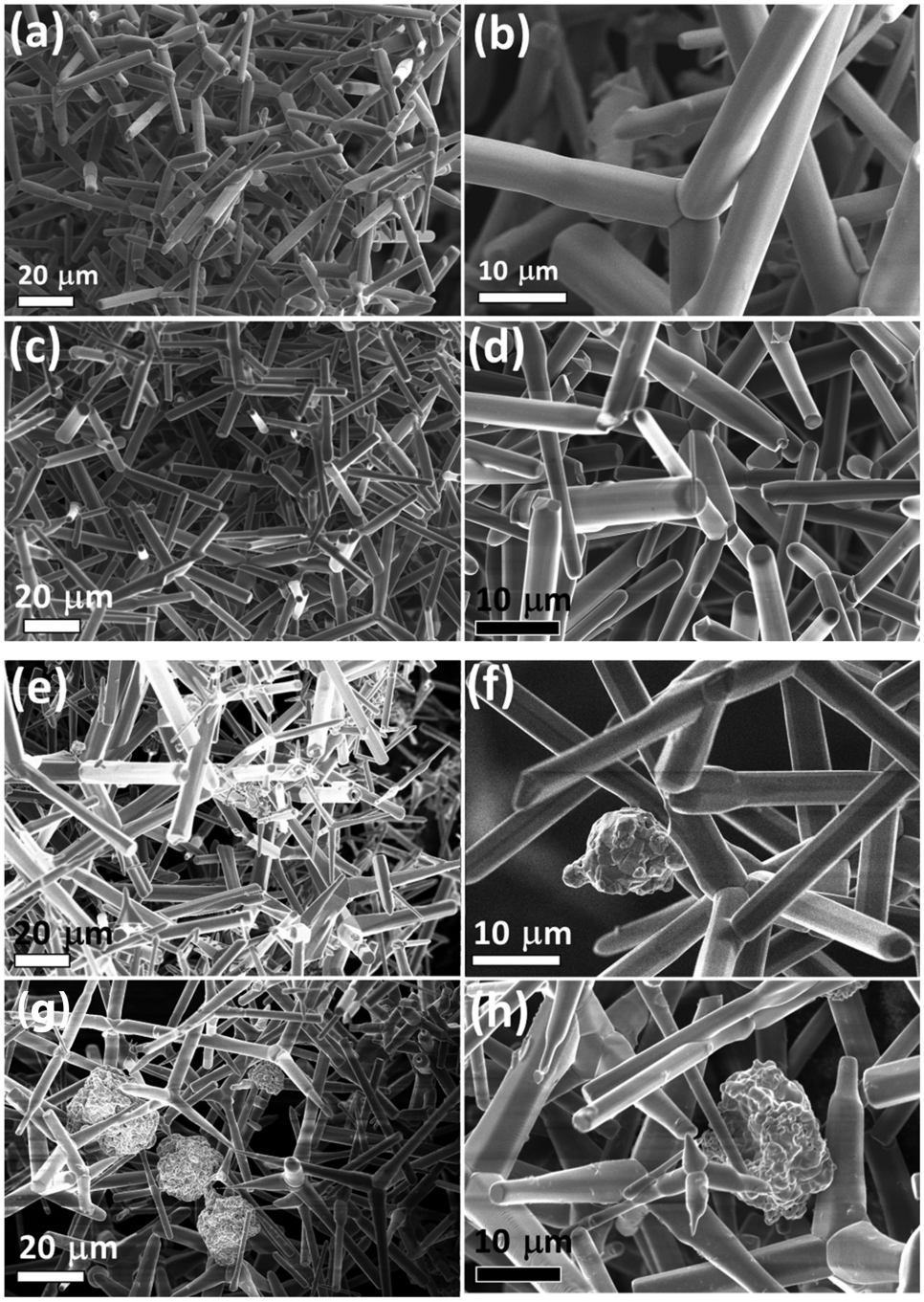

Figure 1. SEM images showing the morphologies of the following hybrid samples at lower and corresponding higher magnification: a,b) ZnO:Bi (20:1); c,d) ZnO:Bi (10:1); e,f) ZnO:Sn (30:1); and g,h) ZnO:Sn (15:1).

presented in **Figure 2**a–d and Figure S4 (Supporting Information), while those for ZnO-T and Zn_2SnO_4 hybrid networks (ZnO:Sn 15:1) are displayed in Figure 2e–h. Independent of the size of the structures (Figure 2a–d and Figure S4, Supporting Information), it can be observed that Bi disperses onto the entire surface of all ZnO tetrapods. Such results were also confirmed by energy dispersive X-ray spectrometry (EDX) line scans taken along the tetrapod arms as well as on ends, which are shown in Figure S5a–d and Figure S5e–h (Supporting Information), respectively. In the ZnO-T-Zn_2SnO_4 hybrid networks, the Sn-oxide was mainly observed in the randomly dispersed additional microsized spherical agglomerates through the network (Figure 2e–h). Furthermore, only a low concentration of Sn-oxide was detected on the ZnO-T surface. Hence, in the case of the ZnO-T-Bi_2O_3 samples, it can be speculated that the absence of spherical agglomerations of microparticles or other types of microstructures reveals that Bi_2O_3 is well-dispersed on the ZnO-T surface, forming a core–shell structure

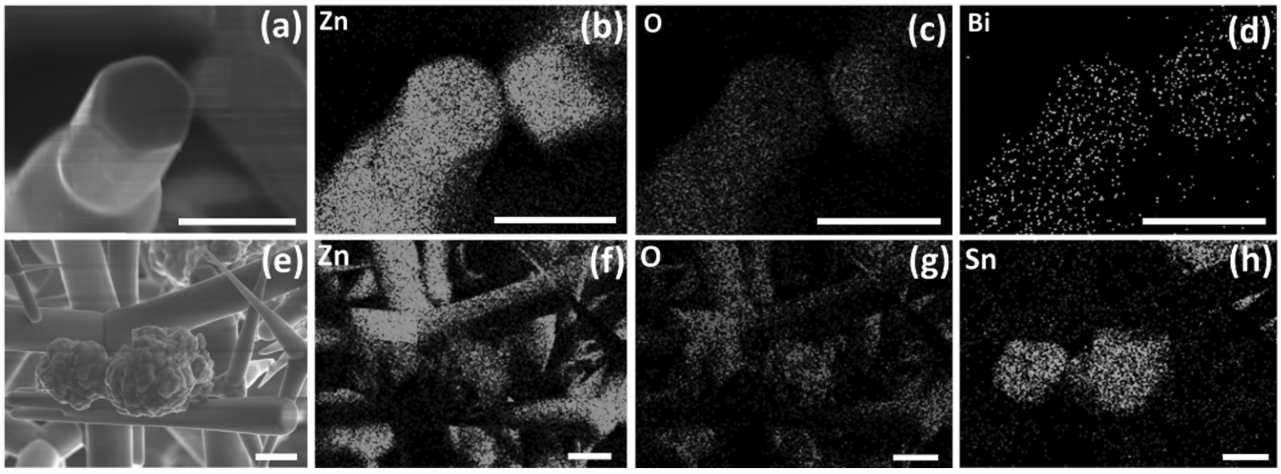

Figure 2. a) SEM image and corresponding elemental mappings b–d) of Bi_2O_3-alloyed ZnO tetrapod arm (ZnO:Bi 20:1) by energy dispersive X-ray spectrometry: b) Zn Lα1_2; c) O Kα1; and d) Bi Mα1. e) SEM image and corresponding elemental mappings f–h) of Zn_2SnO_4-alloyed ZnO tetrapod hybrid networks (ZnO:Sn 15:1) by energy dispersive X-ray spectrometry: f) Zn Lα1_2; g) O Kα1; and h) Sn Lα1. Scale bars for all images are 5 µm.

and a tetrapodal network. Figure S6 (Supporting Information) shows the EDX spectrum of the spherical microparticles from ZnO:Sn (15:1) networks, where peaks of Zn, O, and Sn can be distinguished. The estimated [Zn]:[O]:[Sn] ratio by EDX analysis (see Figure S6, Supporting Information) indicates the formation of Zn_2SnO_4, which was further confirmed by X-ray diffraction (XRD) analysis as shown below.

The structural characterization of the hybrid networks was performed using XRD and Raman spectroscopy techniques. The X-ray diffractograms of ZnO-T hybrid networks with Bi_2O_3 and Zn_2SnO_4 are shown in Figure S7 (Supporting Information). The diffraction maxima assigned to ZnO according to JCPDS PDF Card No. 36-1451 (space group $P6_3mc$ (186)) are marked with "**#**". For the hybrid ZnO-T-Bi_2O_3 3D network, there are two sets of diffraction maxima ascribed to Bi_2O_3 (JCPDS Card No. 10-0244) marked with "**+**" and to ZnO marked with "**#**", respectively (Figure S7a, Supporting Information). Diffraction from the (100), (002), (101), (102), (110), and (103) crystal planes from the ZnO wurtzite structure were detected as the strongest major peaks in the XRD patterns for all the network samples. No significant changes for the characteristic diffraction maxima of ZnO were observed, indicating that the main networks remain stable and the constituting materials are attached to it or covering the entire surface. The XRD pattern of the ZnO-T with the Zn_2SnO_4 hybrid 3D network is shown in Figure S7b (Supporting Information). In addition to the diffraction peaks of ZnO wurtzite, few more diffraction maxima with lower intensities were observed, indicating the presence of the Zn_2SnO_4 cubic-face-centered (CFC) spinel structure described by the $\{F_{d\bar{3}m}(227)\}$ space group and lattice constant a = 0.86574 nm. The diffraction maxima of the zinc stannate were indexed to the JCPDS Card No. 24-1470 and marked on the graph as "**+**". Taking into account that the formation of Zn_2SnO_4 was also demonstrated by XRD investigations in a previous work,[22] one can assume that the added Sn-metal microparticles are oxidizing and transforming into Zn_2SnO_4 during thermal annealing, being described by the following Equations (1)–(3).[8,28]

$$Zn(s) \xrightarrow{\Delta} Zn(g) \quad (1)$$

$$Sn(s) \xrightarrow{\Delta} Sn(g) \quad (2)$$

$$2Zn(g) + Sn(g) + 2O_2 = Zn_2SnO_4(s) \quad (3)$$

Thus, following this assumption, the Zn_2SnO_4 is formed by the interaction of Zn and Sn vapor.[8,28] Also, Zn_2SnO_4 is in the form of closely packed oxygen ions and rutile chains connected by cations in the tetrahedral sites, and these chains are conduction paths for electrons due to unoccupied orbitals of the cations that overlap in the rutile.[29]

2.3. Micro-Raman Study of Hybrid 3D Networks

Figure 3a,b shows the room-temperature (RT) micro-Raman spectra of the ZnO-T hybrid networks with (a) Bi_2O_3 (ZnO:Bi 20:1) and (b) Zn_2SnO_4 (ZnO:Sn 30:1). Due to the random distribution of the secondary phases in ZnO-T, the Raman spectra were measured at different points of the hybrid networks. In the case of the ZnO:Bi (20:1) samples, all the detected peaks can be assigned to the typical active modes belonging to first and second-order Raman scattering of the ZnO wurtzite structure (see Figure 3a).[30] While discussing the Raman spectra of these ZnO-T structures, different aspects need to be considered as follows. The wave-vector conservation restricts the phonons involved in first-order Raman scattering to those near $k \approx 0$ and depends on incident and scattering geometry relatively to the principal axis of the ZnO crystal, resulting in a shift in the frequencies of the transverse (TO) and longitudinal (LO) modes. In addition, a mixing character between A_1 and E_1 polar modes may occur when the incident beam propagates in a direction that is not aligned with the axis of the ZnO crystal; moreover, a shift in the frequencies of the TO and LO modes can be observed.[31] Furthermore, when activated by disorder, phonons from the entire Brillouin zone participate

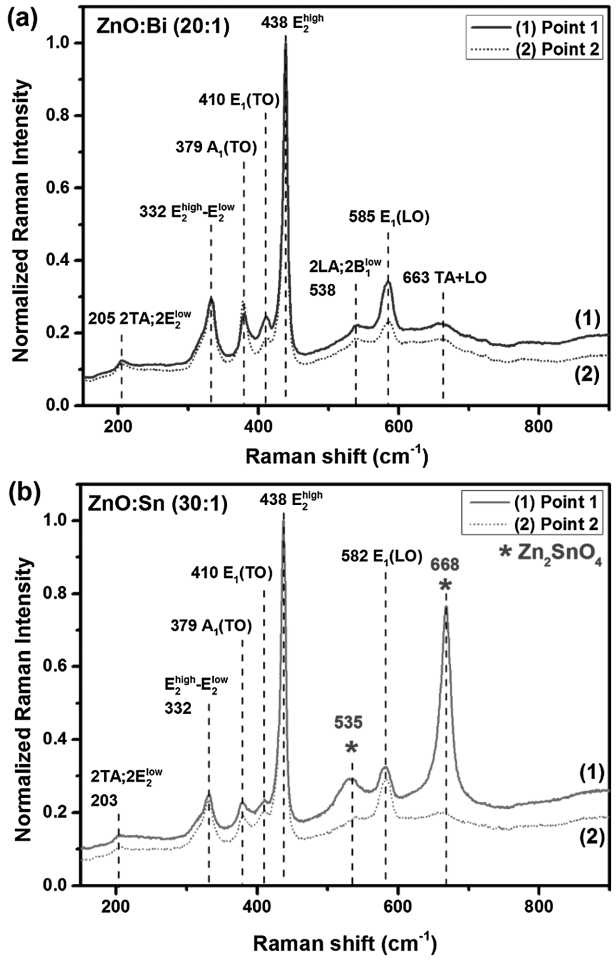

Figure 3. Room-temperature micro-Raman spectra of the ZnO-T with a) Bi_2O_3 (ZnO:Bi 20:1) and b) Zn_2SnO_4 (ZnO:Sn 30:1) hybrid networks. A 442 nm laser line was used as excitation source.

in second-order Raman scattering, leading to a rich spectrum like the one observed in Figure 3a. The second-order Raman is determined by both the phonon density of states and the selection rules of the two-phonon scattering processes. The similarity of the Raman spectra from different regions indicates a homogenous distribution of the defects in the ZnO lattice. In the β-Bi_2O_3 phase, we observed three bands at about 128, 317, and 462 cm^{-1}, corresponding to Bi—O stretches as reported.[32] However, regardless of the analyzed region of the ZnO:Bi (20:1) sample, none of the Raman bands detected can be assigned unambiguously to the β-Bi_2O_3 phase. We interpret these results as a consequence of the superposition of two effects: (i) the high laser depth penetration relative to the thickness of the β-Bi_2O_3 layer over the ZnO-T structures, and (ii) the strong intensity of the second-order Raman scattering from ZnO.

In a similar way, the main vibrational frequencies of the hybrid network of ZnO-T with zinc stannate were assigned to the ZnO crystal lattice (see Figure 3b), and the main aspects discussed above regarding the contribution of the ZnO-T structures remain valid to interpret the Raman spectra of Figure 3b. Depending on the analyzed region of the sample (ZnO:Sn 30:1), in addition to the ZnO Raman bands, two further well-defined vibrational modes with peaks at 535 and 668 cm^{-1} were also observed. The Raman band at 668 cm^{-1} matches the vibrational modes reported for the crystalline spinel structure of Zn_2SnO_4,[33,34] already identified by XRD results, and is assigned to the mode of A_{1g} symmetry of the Zn_2SnO_4 spinel structure.[35] Despite the Raman band at 535 cm^{-1} being at a higher frequency than the reported values for the E_{2g} mode of Zn_2SnO_4,[33,35] we consider this band related to this crystalline phase. We believe that the broadening of this Raman band and the frequency shift is due to the overlap with the LA and B_1 modes of ZnO. Concerning the detection of the Zn_2SnO_4 Raman bands, the dependence of the micro-Raman spectra on the probed sample region agrees with a non-uniform distribution of the Zn_2SnO_4 phase, as was observed by SEM (see Figure S3, Supporting Information).

2.4. Photoluminescence Study of the Hybrid 3D Networks

Figure S8 (Supporting Information) shows room-temperature (RT) absorbance and photoluminescence excitation (PLE) spectra of the ZnO-T with Bi_2O_3 (ZnO:Bi 20:1) and Zn_2SnO_4 (ZnO:Sn 30:1) hybrid 3D networks, respectively. The PLE was monitored at the PL maxima as discussed in Text S2 (Supporting Information). In order to evaluate the RT PL properties of the ZnO-T with Bi_2O_3 (ZnO:Bi 20:1) and Zn_2SnO_4 (ZnO:Sn 30:1) hybrid networks, excitation energy-dependent PL measurements were realized as shown in Figure S9 (Supporting Information). It can be observed that a strong green band emission with a maximum at ≈2.4 eV is present for the studied network samples. However, the spectral shape of the broad emission band was found to be dependent on the excitation energy used. A decrease of the green-band full width at half maximum (FWHM) was found to occur by decreasing the excitation energy, in particular for energies below the ZnO bandgap. Such a tendency suggests that the observed green PL is due to an overlap of emitting centers rather than a single one. On the other hand, and corroborating the PLE discussion (see Text S2, Supporting Information), the data also indicate that the low-energy excitation bands are likely to be originating from crystalline phases other than ZnO. The same spectral shape and peak positions are expected if the green band is due to the same defect in the ZnO host, which could be excited by energy above and below the material bandgap. Since this is not the case, the excitation bands (Figure S8, Supporting Information) are believed to originate from Bi_2O_3 and Zn_2SnO_4 phases, which are responsible for the green luminescence observed in such materials and commonly associated with intrinsic defects (e.g., oxygen vacancies).[36,37] In the ZnO host, the chemical nature of the defect responsible for the green band has been widely debated in the literature, where its relation to intrinsic defects and their complexes is one of the most likely explanations considered.[38] However, some of these intrinsic defects are known to have high formation energies and are unlikely to occur. This is the case for an oxygen vacancy (V_O) in ZnO, which leads to a deep donor located at ≈1.0 eV below the conduction band.[39] On the other hand, unstable zinc interstitials, Zn_i, give rise to shallow donors with low migration energies, which are therefore fast diffusers.[39] Among the intrinsic defects in ZnO, zinc vacancies (V_{Zn}) and oxygen interstitials (O_i) result in deep acceptors.[40] Apart from its association with the

recombination of intrinsic defects and surface defects,[38] some authors argue that the structured green band observed in ZnO at low temperatures is due to extrinsic impurities such as Cu.[41] Furthermore, the observed modulation of the visible broadbands have also been discussed on the basis of the whispery gallery modes (WGM) typically observed in micro-nanostructured optical resonators and ZnO needles.[42] In order to evaluate the spectroscopic features of ZnO-T with the Bi_2O_3 (ZnO:Bi 20:1) and Zn_2SnO_4 (ZnO:Sn 30:1) hybrid networks, the samples were cooled down to 10 K and the temperature-dependent PL spectra between 10 K and RT were measured under 3.8 eV photon excitation, as presented in Figure S10 (Supporting Information). The used excitation conditions are above the bandgap energies for ZnO, Bi_2O_3, and Zn_2SnO_4. Therefore, we are able to simultaneously observe the recombination processes from the different hosts. The low-temperature PL result reveals that both samples exhibit the structured green emission at ≈2.4 eV, which was earlier reported by Dingle.[41] Therefore, with the used excitation conditions, the main observed PL is due to the recombination in the ZnO host. In the case of the ZnO-T with Bi_2O_3 (ZnO:Bi (20:1) network), a well-defined, structured near-band-edge recombination (Figure S10a, Supporting Information) is observed due to donor-bound excitons (D^0X), two electron satellites (TES), and surface defects.[18,43] With an increase in the temperature, a general decrease of the PL intensity is observed due to nonradiative processes, which compete with the radiative ones. In particular, the thermal quenching of the D^0X recombination is evidenced through the dissociation of the exciton complex, releasing free carriers to the bands. On the other hand, for the ZnO-T with Zn_2SnO_4 (ZnO:Sn (20:1) network), no shallow level recombination was detected even at low temperatures, where the main emission is mediated through deep level recombination. Increasing the temperature of samples may allow the identification of the nature of the green band (shown at RT in Figure S9, Supporting Information), when the constituting oxides of the hybrid network are simultaneously excited. The behavior with the increase in temperature of the peak position and spectral shape of the green band is different from that expected for a single emitting defect. This result shows that the green emission is composed of an overlap of emitting centers in the same spectral band originating from ZnO, Bi_2O_3, and Zn_2SnO_4 phases.

2.5. Gas Sensing Properties of Hybrid ZnO-T-Bi_2O_3 and ZnO-T-Zn_2SnO_4 3D Networks

Figure 4a shows the gas sensing results of ZnO-T-Bi_2O_3 (ZnO:Bi 20:1) hybrid networks. It can be seen that at an operating temperature (OPT) of 400 °C the sensor structures demonstrated a good selectivity to H_2 gas with a gas response of $S_{H2} \approx 8$, while the gas response to CO and ethanol vapors at the same operating temperature was 2 and 2.6, respectively. We note that these values are higher compared to pristine ZnO-T networks (see inset in Figure 4a). A gas response to CH_4 gas was not observed for these samples. The resulting selectivity factors at an operating temperature of 400 °C are $S_{H2}/S_{EtOH} \approx 4$ and $S_{H2}/S_{CO} \approx 3$. The optimal operating temperature for EtOH vapor is 350 °C with a response $S_{EtOH} \approx 3$. While the optimal operating temperature of the CO gas is 400 °C, as for H_2 gas, the sensor structure exhibits the lowest gas response of $S_{CO} \approx 2$. For samples with a higher content of Bi-metal microparticles (ZnO:Bi 10:1), inferior gas sensing performances were observed compared to ZnO:Bi (20:1) samples (Figure S11a, Supporting Information). The gas response did not reach values higher than 1.5 and the sensitivity and selectivity to H_2 gas were decreased considerably ($S_{H2} \approx 1.5$, $S_{H2}/S_{EtOH} \approx 1.1$, and $S_{H2}/S_{CO} \approx 1.2$). Due to poor stability with a slow response and recovery (Figure S11b, Supporting Information), we excluded the ZnO:Bi (10:1) samples from further investigations. All studied ZnO:Bi samples demonstrated a characteristic p-type sensing response (namely, a decrease in current under exposure to reducing gases). The related sensing mechanism will be further discussed in the following sections.

Figure 4b shows the data of the gas response versus the operating temperature of the ZnO-T with Zn_2SnO_4 (ZnO:Sn 30:1) hybrid networks based sensor. In the case of all studied ZnO:Sn samples, an n-type sensing behavior was observed (increase in resistance after exposure to reducing gases, as well as for pristine ZnO-T networks, see inset in Figure 4a). The highest gas response was obtained for CO gas, $S_{CO} \approx 29.3$, at 275 °C operating temperature. The gas response to H_2 gas and CH_4 gas at the same OPT was 2.3 and 1.8, respectively. These results demonstrate a high selectivity of the ZnO-T-Zn_2SnO_4 (ZnO:Sn 30:1) hybrid networks to CO gas at 275 °C operating temperature. The optimal OPT for H_2 gas is 250 °C with $S_{H2} \approx 4.11$, while for ethanol vapors and CH_4 gas the optimal OPT are 225 and 275 °C, with $S_{EtOH} \approx 1.54$ and $S_{CH4} \approx 1.8$, respectively. The selectivity factors for CO gas at optimal OPT (275 °C) are $S_{CO}/S_{H2} \approx 12.7$, $S_{CO}/S_{EtOH} \approx 29.3$, and $S_{CO}/S_{CH4} \approx 16.3$.

Similar to the case of the ZnO-T-Bi_2O_3 hybrid networks-based sensor structures, ZnO-T-Zn_2SnO_4 networks with higher concentration of Sn-metal microparticles (ZnO:Sn 15:1) reveal lower gas response when compared to ZnO:Sn (30:1) samples (see Figure S11c, Supporting Information). The optimal operating temperature remained at the same values for all tested gases, with the exception of EtOH-ethanol vapor, due to complete reduction in gas response. The response to H_2 gas of the ZnO:Sn (15:1) samples decreased about three times in comparison with ZnO:Sn (30:1) samples ($S_{CO} \approx 9$ vs $S_{CO} \approx 29.3$). Besides the decrease in gas response, a considerable increase in response time (τ_r) and recovery time (τ_d) for ZnO:Sn (15:1) samples was observed (see Table S1 and Figure S11d, Supporting Information). Thus, ZnO-T-Zn_2SnO_4 networks with higher concentration of Sn metal microparticles (ZnO:Sn 15:1) were excluded from further investigations.

The gas response versus gas concentration (in ppm) was also investigated for ZnO-T-Bi_2O_3 (ZnO:Bi 20:1) and ZnO-T-Zn_2SnO_4 (ZnO:Sn 30:1) hybrid 3D networks. Results for gas response versus H_2 gas concentration for ZnO-T-Bi_2O_3 and gas response versus CO gas concentration for ZnO-T-Zn_2SnO_4 hybrid networks are presented in Figure 4e,f, respectively (in the log vs log plot). The respective slope values were determined from linear fitting of the curves (see Figure 4e,f). Also, the sensitivity of sensors was calculated and included in Table S1 (Supporting Information).

In order to determine the rapidity of the sensors, the response and recovery times (defined as the time required for

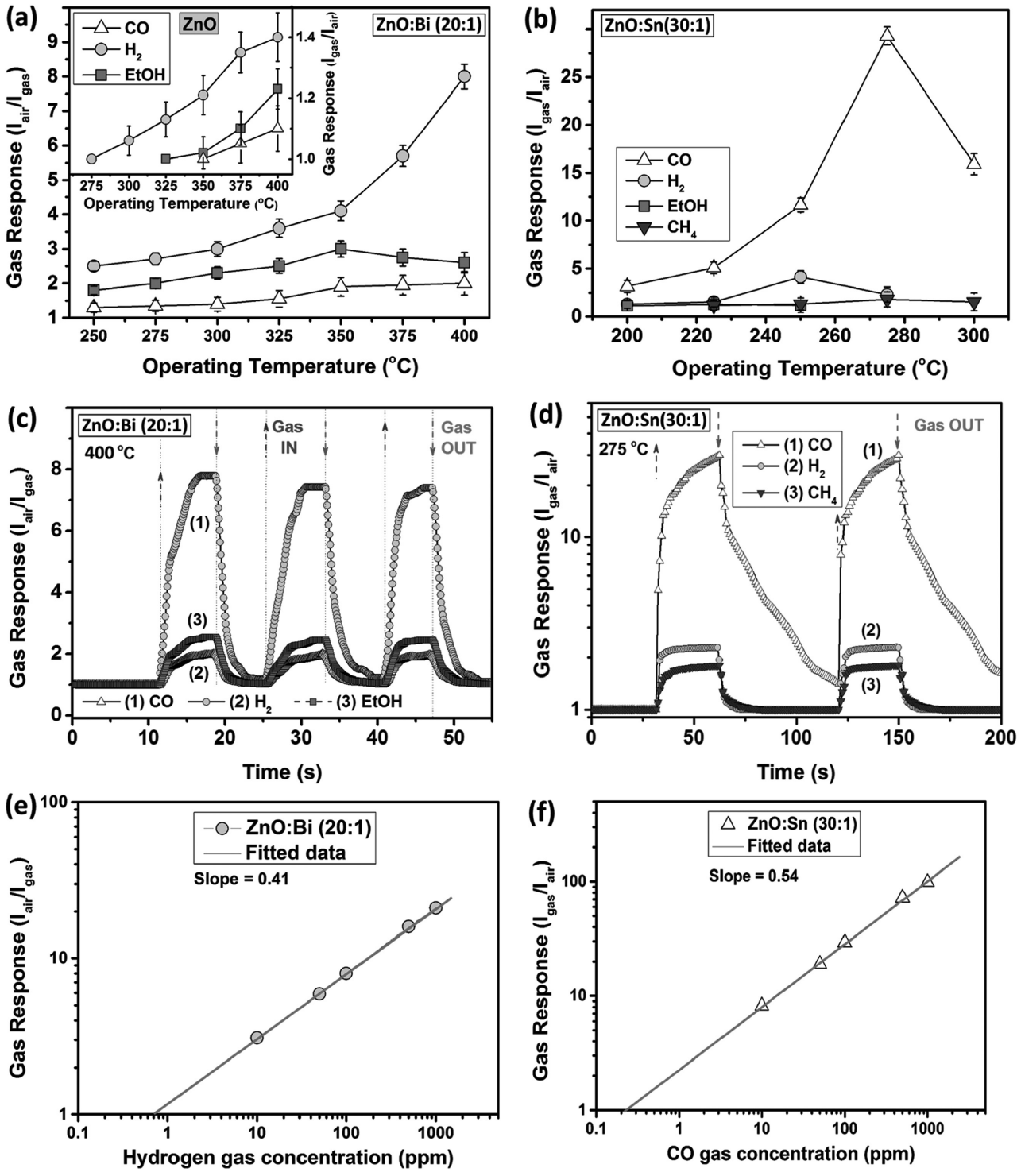

Figure 4. Gas response versus operating temperature for a) Bi_2O_3-alloyed ZnO-T hybrid networks (ZnO:Bi 20:1) (in inset results for the pristine ZnO-T networks are presented) and b) Zn_2SnO_4-alloyed ZnO-T hybrid networks (ZnO:Sn 30:1). Transient response of the c) Bi_2O_3-alloyed ZnO-T hybrid networks (ZnO:Bi 20:1) to reducing gases at 400 °C operating temperature and d) Zn_2SnO_4-alloyed ZnO-T hybrid networks (ZnO:Sn 30:1) to reducing gases at 275 °C operating temperature. Gas response of hybrid networks versus concentration of hydrogen gas: e) Bi_2O_3-alloyed ZnO-T (ZnO:Bi 10:1) and f) Zn_2SnO_4-alloyed ZnO-T (ZnO:Sn 30:1).

the response to obtain 90% of the final response and recovery values, respectively) were calculated from the transient gas response of the ZnO:Bi (20:1) and ZnO:Sn (30:1) at their optimal operating temperature (see Figure 4c,d). The calculated values are presented in Table S1 (Supporting Information). As can be observed, ZnO-T with Bi_2O_3 hybrid networks

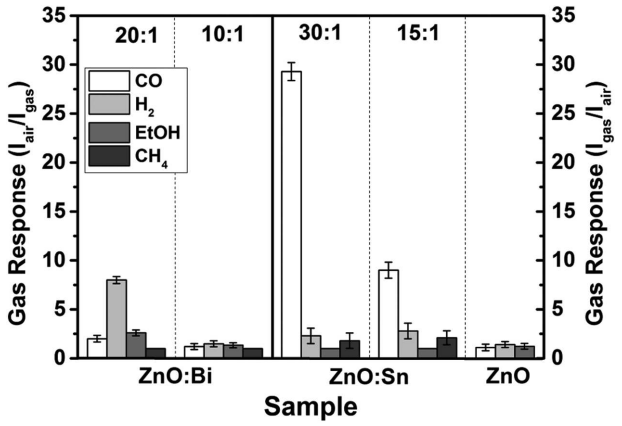

Figure 5. Gas response versus type of the samples studied at their optimal operating temperature: ZnO:Bi—400 °C; ZnO:Sn—275 °C; and ZnO—400 °C.

demonstrated faster response and recovery times. Furthermore, by an increase of the concentration of metal microparticles for both types of samples (ZnO:Bi and ZnO:Sn), a decrease in rapidity of the sensors can be observed.

Figure 5 shows a compilation of the results on the gas response of the studied sensor samples at their optimal operating temperature. Consequently, samples with higher density of metal particles in the network precursors demonstrate inferior gas sensing properties. Also, evident differences in selectivity of the samples, in dependence of added metal microparticles were observed. ZnO:Bi (20:1) hybrid networked samples showed good selectivity to H_2 gas at 400 °C operating temperature, the same as the pure ZnO-T networks,[8] but with improved gas response. In the case of ZnO-T-Zn_2SnO_4 hybrid networks, an excellent selectivity to CO gas was achieved, especially for samples with lower density of tin oxide microparticles. It has been demonstrated that there exists a possibility to change/tune the selectivity of the ZnO-T networks, as in the case of ZnO-T with Fe_2O_3, CuO, and $ZnAl_2O_4$ networks.[22] The related gas sensing mechanism will be further discussed in the next section.

The main advantages of the developed hybrid 3D networks are high porosity and anti-agglomeration properties that facilitate the diffusion of gas molecules to the tetrapods' arms (leading to a higher and rapid sensitive response) and the possibility to tune the sensors' selectivity by adequate and rational selection of added metal microparticles. Thus, taking into account the catalytic effect of other semiconducting oxides and the influence of different formed heterostructures, the formation of unique and novel hybrid structures can be realized. In this work, even with the size of tetrapods in micrometric range, through the hybridization with Bi_2O_3 and Zn_2SnO_4 it was possible to obtain high-performance sensors for selective detection of H_2 and CO gases, respectively.

2.6. The Gas Sensing Mechanism Proposed for the Hybrid 3D Networks

The discussion of conduction mechanisms of the hybrid sensor structure and the gas sensing mechanisms is supported by the measured experimental data. The energy band diagrams of the promoted heterojunctions based on the ZnO-T with Bi_2O_3 and on the ZnO-T with Zn_2SnO_4 semiconductors are depicted in Figure S12 (Supporting Information). From SEM, XRD, EDX, Raman, and sensing investigations, the following conclusions can be formulated: (i) p-Bi_2O_3 is well dispersed on the surface of ZnO-T, giving rise to p-p homojunctions between different ZnO-T arms of the neighboring tetrapods, resulting in the p-type gas sensing behavior of the samples; (ii) n-Zn_2SnO_4 micro- and nanostructures form additional Zn_2SnO_4-ZnO heterojunctions, which contribute to an improvement in the sensing properties of the samples.[44–47]

Figure 6a illustrates the schematic gas sensing mechanism of the ZnO-T-Bi_2O_3 hybrid networks. Due to a relatively thick layer of Bi_2O_3 on the surface of the ZnO-T arms (in the range of 300–400 nm, see Figure S13, Supporting Information), the electrical conduction will occur mainly through the hole accumulation layer (HAL) created on the Bi_2O_3 surface, while Bi_2O_3/ZnO-T do not participate in surface reactions.[15–17] This phenomenon is specific for semiconductors with p-type conductivity, and the related gas sensing mechanism has also been proposed earlier.[15–17] Since modulation of the potential barriers at grain boundaries is excluded, as it occurs in the case of n-type semiconductors, modulation of HAL width is responsible for the variation in resistance of the sensor structure under exposure to the tested gases (see Figure 6a).[15–17] At exposure to ambient air (in air, see Figure 6a), the oxygen atomic species are chemisorbed onto the surface of the Bi_2O_3 layer, which creates the HAL region ($\frac{1}{2}O_2(g) \leftrightarrow O^-(ads) + h^+$)[17] with relatively lower resistance compared to the core region of ZnO. Thus, the current will flow mainly through the HAL region created at the Bi_2O_3/ZnO-T surface. At exposure to H_2 gas, the oxidation of H_2 molecules ($H_2(g) + O^-(ads) + h^+ \rightarrow H_2O(g)$)[15] will take place, and due to the released electrons the width of HAL regions will decrease (in H_2, see Figure 6a). Consequently, the current through the HAL region decreases according to gas sensing investigations (see Figure 5c and Figure S11b, Supporting Information). Bi_2O_3 p-type materials and their composites have not been investigated as intensively as ZnO and SnO_2,[48] and only a few reports are available in the literature[44,49] on their gas sensing behavior towards reducing gases. Very few studies have demonstrated good H_2 gas response at relatively high operating temperatures but with lower response speed,[44,49] which could explain the improved sensing properties of the ZnO-T-Bi_2O_3 hybrid 3D networks and the decrease in rapidity (speed of response) as compared to that of pure ZnO-T 3D networks.

In the case of ZnO-T-Zn_2SnO_4 hybrid networks, the improved CO gas sensing properties can be explained as below. Due to the additionally formed Zn_2SnO_4/ZnO-T heterojunctions (see Figure S12b, Supporting Information), more potential barriers appear that lead to a more efficient resistance modulation of the sensor under exposure to the tested gas (see Figure 6b). Thus, two mechanisms are involved in the gas detection process, namely, modulation of the potential barriers between ZnO-T arms (described in a previous work for ZnO-T networks[8]) and at Zn_2SnO_4/ZnO-T heterojunctions (bi-functional sensing mechanism,[25,50] see Figure 6b). The ΔV_b (air) is related to chemisorption of oxygen species upon exposure to air of the

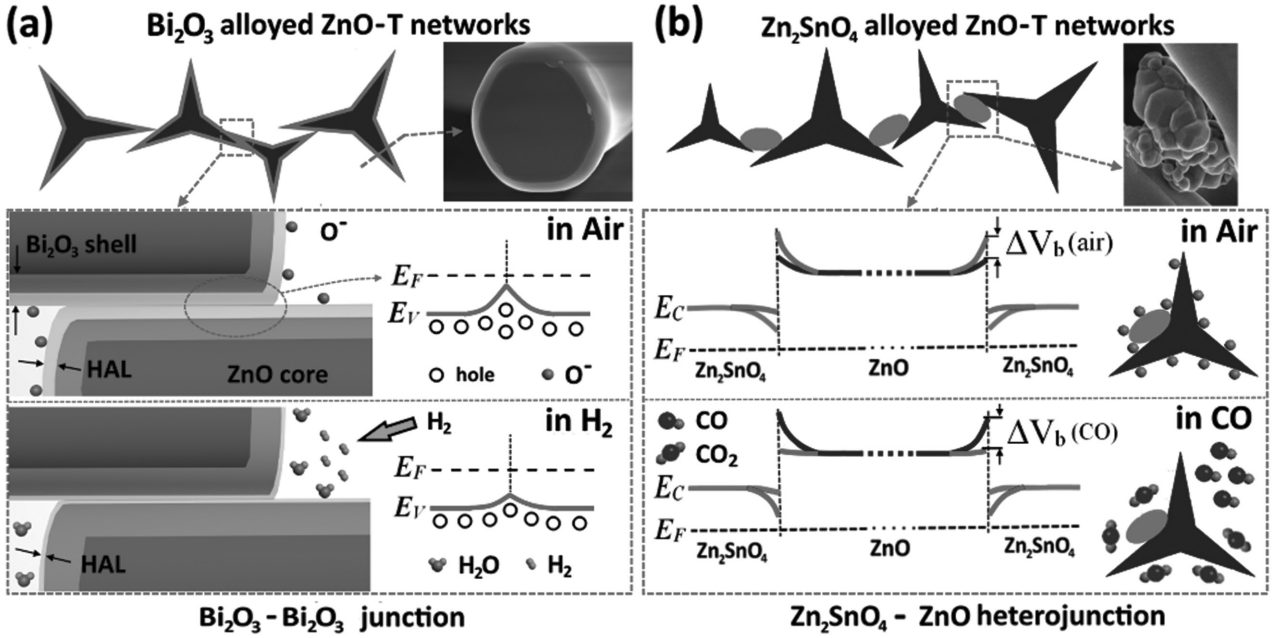

Figure 6. Illustration of proposed gas sensing mechanism for ZnO-T hybrid networks alloyed with: a) Bi_2O_3 and b) Zn_2SnO_4; at exposure to ambient air and to test gases (H_2 for ZnO:Bi and CO for ZnO:Bi).

ZnO-T-Zn_2SnO_4 hybrid 3D networks to air (in Air, Figure 6b). Upon exposure to CO gas ($CO(g) + O^-(ads) \rightarrow CO_2(g) + e^-$),[46,47,51] the heights of the potential barriers are decreasing (ΔV_b (CO) due to released electrons (in CO, Figure 6b), leading to an improved modulation in resistance of the hybrid networks.[50,51] Improved selectivity of ZnO:Sn samples to CO gas can be explained based on gas sensing investigations of other Zn_2SnO_4-ZnO sensors, which have also demonstrated high sensitivity and selectivity to CO gas.[46,47,51–53] However, the higher density of the Zn_2SnO_4 microparticles leads to a formation of agglomerates in the hybrid networks and hence to a decreased porosity (see Figure 1), which leads to a lower gas response, but an almost identical selectivity, as observed in the experimental data.

2.7. Sensor Devices Based on a Single Structure and Its Sensing Mechanism

Several devices have been fabricated based on individual tetrapod arms (ZnO-T-Bi_2O_3 and ZnO-T-Zn_2SnO_4) with different diameters and lengths hereafter designated as Bi1, Bi2, and Bi3 (for ZnO-T-Bi_2O_3 samples), and as Sn1 and Sn2 (for ZnO-T-Zn_2SnO_4 samples). The geometrical parameters of the devices based on ZnO-T-Bi_2O_3 and ZnO-T-Zn_2SnO_4 arms are presented in Table S2 (Supporting Information). All the devices were tested to UV light and various gases. The devices based on a single ZnO-T-Bi_2O_3 arm showed poor UV response (see Figure S14, Supporting Information), but interesting results on H_2 gas sensing were obtained. **Figure 7**a shows the current–voltage characteristic of the device Bi2, based on a single ZnO-T-Bi_2O_3 arm, where the inset presents a SEM image of the fabricated and studied device. This device exhibits a high H_2 gas response (≈70) at room

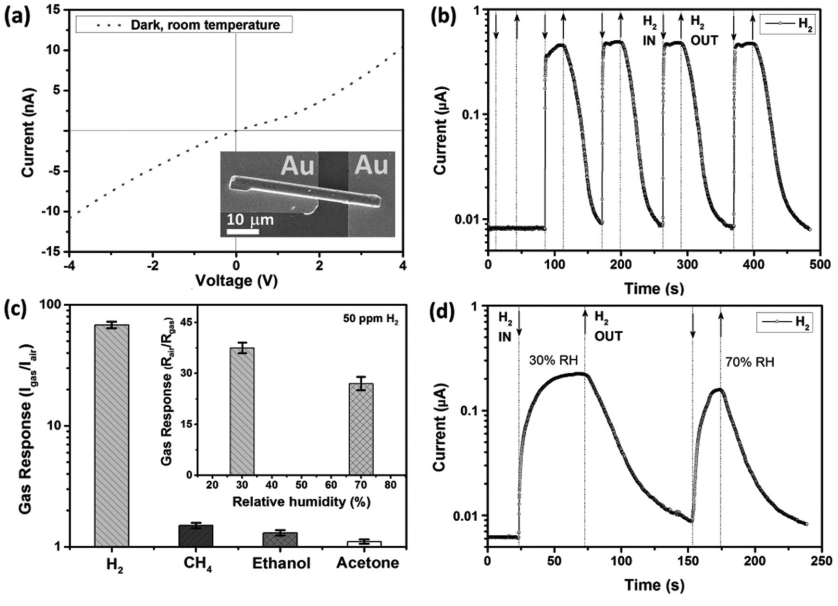

Figure 7. a) The current–voltage characteristic of the device based on a single ZnO-T-Bi_2O_3 arm (device Bi2) measured at room temperature in the dark. b) Dynamic H_2 gas (100 ppm) response measured at room temperature. c) Gas response to different types of gases and vapor measured at room temperature (concentration of all gases—100 ppm). In the inset, data for the gas response to 50 ppm H_2 gas at ≈30% RH and ≈70% RH are shown. d) Dynamic gas response to 50 ppm H_2 gas at 30% RH and 70% RH.

temperature with good repeatability (see Figure 7b). The selectivity compared to other gases was also tested (see Figure 7c), and despite a negligible gas response (<1.5) to CH_4, ethanol, and acetone, the device provides an excellent selectivity to H_2 gas at room temperature. The influence of relative humidity (RH) under sensing device parameters is another important factor since water vapor is present in most real applications.[54] Therefore, all the devices developed in this work were tested at ambient 30% RH, whereas device Bi2 was tested at ambient 30% RH and at 70% RH (see inset in Figure 7c,d and Table S4, Supporting Information). A decrease in sensitivity by about 25%, that is, from ≈36 to ≈27 (for 50 ppm H_2 gas, see Table S4, Supporting Information), is observed and can be explained on the basis of the competition among the adsorbed oxygen molecules onto the surface of the tetrapod's arm between H_2O and H_2.[17,55] The response times (τ_r) and recovery times (τ_f) were calculated under different conditions and are summarized in Table S4 (Supporting Information). For 100 ppm H_2 gas the respective values are ≈3.5 and ≈25 s, which are comparable with one of the best results reported in the literature, even at higher operating temperatures (see **Table 1**). Compared to results from the ZnO-T-Bi_2O_3 hybrid networks, the gas response of a single tetrapod arm is much better (≈9 times higher) although the response time is comparable, and the recovery time of the networks is faster due to a higher operating temperature (400 °C). Figure S15 (Supporting Information) shows the gas response versus concentration of H_2 gas. The lowest detection limit of 1 ppm can be approximated from this graphic (see Figure S15, Supporting Information) by linear fitting and the response criteria of $R_{air}/R_{gas} > 1.2$.

The other devices based on single ZnO-T-Bi_2O_3 with different geometrical parameters of the tetrapod's arm (see Table S2, Supporting Information) were tested as well (that is, Bi1 and Bi3). A SEM image of the Bi1 device is presented in the inset of Figure S14 (Supporting Information), while the one of device Bi3 is shown in the inset of Figure S16 (Supporting Information). Figure S16 (Supporting Information) shows the dynamic H_2 response of the Bi1 and Bi3 devices at room temperature. Calculated gas responses with τ_r and τ_d values are summarized in Table S4 (Supporting Information). These devices demonstrated more inferior parameters. For example, device Bi3 showed a long recovery time with relatively low gas response, while device Bi1 showed a high instability and a low repeatability. However, the gas response value is still higher than for pristine ZnO microwire- and nanowire-based devices reported earlier by Lupan et al.[1,18,48,56]

For the devices based on ZnO-T-Zn_2SnO_4 arms, that is, for device Sn1 (see Figure S18, Supporting Information), poor UV and gas sensing properties were obtained. However, more interesting sensing properties were observed for device Sn2 based on a single tetrapod (see **Figure 8**a), which showed single Schottky contact (see Figure S19, Supporting Information). Figure S20 (Supporting Information) shows the dynamic UV response of device Sn2 under different applied bias voltages, that is, −10, −1, +1, and +10 V. The calculated UV response and time constants are presented in Table S3 (Supporting Information). The highest UV response was obtained at −10 V, but with incomplete recovery to the initial electrical baseline.

In the case of H_2 gas exposure a considerable increase in the current value was observed (see Figure 8b). As was the case for UV exposure, the highest response was obtained under a negative applied bias of −10 V, with $I_{gas}/I_{air} \approx 300$. Under an applied bias voltage of +10 V the gas response was much lower ($I_{gas}/I_{air} \approx 25$). The calculated response and recovery times for both applied bias voltages are presented in Table S5 (Supporting Information). As can be observed, under a negative applied bias, the recovery time is much shorter.

Table 1. Comparison of the parameters for CO and H_2 gas sensors based on different semiconducting metal oxides.

Sensing material	CO conc. [ppm]	H_2 conc. [ppm]	R_{gas}/R_{air}	OPT [°C]	τ_r [s]	τ_d [s]	Year
CuO-ZnO core–shell nanowires[57a]	10	–	≈6.5	300	–	–	2016
Nanostructured Co_3O_4[52]	25	–	≈2.2	200	>300	58	2015
Pd decorated ZnO nanorod arrays[57b]	100	–	≈4.5	300	≈200	≈300	2012
CuO-ZnO composite nanowire array[58]	300	–	7.6	300	26	1048	2011
Zn_2SnO_4:Cu[46]	200	–	≈14	350	–	–	2000
ZnO/Zn_2SnO_4 layered type[59]	200	–	≈8	380	–	–	2001
ZnO-T with Zn_2SnO_4 hybrid networks (ZnO:Sn 30:1)	100	–	≈29.3	275	22.7	25.6	**This Work**
ZnO-SnO_2 composite nanofibers[50]	–	0.1	78	350	74	289	2009
$Zn_xCu_{1-x}O_y$ nanocrystalline films[17]	–	100	≈10.6	300	≈2	≈5.5	2016
ZnO-T networks[8]	–	100	1.62	400	0.08	0.18	2015
ZnO:Ag single NW[56]	–	100	1.6	30	22	11	2016
ZnO-T with Bi_2O_3 hybrid networks (ZnO:Bi 20:1)	–	100	8	400	5.3	3.9	This Work
Single Cd-doped ZnO NW[5]	–	100	≈3.8	RT	14	11	2012
A single ZnO-T-Bi_2O_3 arm (Bi2)	–	100	70	RT	3.52	25	**This Work**
A single ZnO-T-Zn_2SnO_4 arm (Sn2)	–	100	294	RT	11.7	34.5	**This Work**

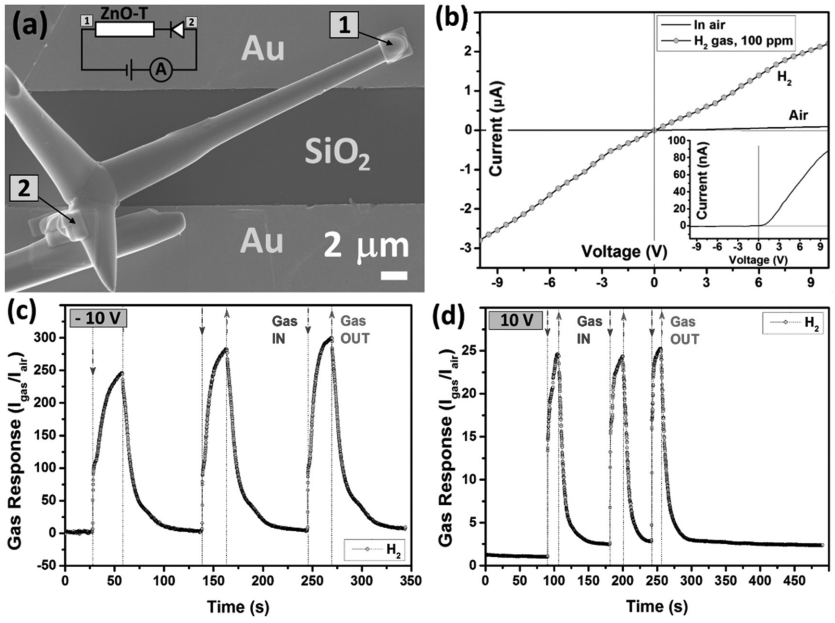

Figure 8. a) SEM image of the device Sn2, based on a single ZnO-T-Zn_2SnO_4 tetrapod. The inset shows the schematic structure of the device Sn2. b) Current–voltage characteristic in air and under H_2 gas exposure (100 ppm) of the device Sn2. The inset presents the current–voltage characteristic in air for better visualization of a single Schottky contact. Dynamic H_2 response of the device Sn2 with single Schottky contact at applied bias: c) −10 V and d) +10 V.

Figure S21 (Supporting Information) shows the overall process of ZnO-T integration into the device from dispersion of the ZnO-T-Zn_2SnO_4 networks to transfer onto the SiO_2/Si substrate. While one arm of the tetrapod (noted as 1, see Figure 8a) is placed onto one Au/Cr pad and in contact with Pt, another contact (noted as 2, see Figure 8a) is located in air without contact to the Au/Cr pad but still in contact with Pt. The work function of Pt at 6.1 eV is higher than that of ZnO, and a Schottky barrier (SB) is thus formed at contact 2 (Figure S22a, Supporting Information).[60] The gas sensing mechanism based on SB is presented in Text S3 (Supporting Information).

Table 1 summarizes the performances of the developed sensors in comparison with some of the best results reported in the literature for CO and H_2 gas sensors. It is clear that the developed CO gas sensors based on ZnO-T with Zn_2SnO_4 networks show excellent gas sensing properties, while H_2 gas sensors based on ZnO-T with Bi_2O_3 networks exhibit lower gas response compared to the other results, although the response rapidity of the sensors is relatively fast. In the case of sensors based on a single structure (Bi2 and Sn2), an excellent ultra-high gas response was obtained at room temperature.

2.8. DFT Calculations of H_2 and CO Gas Molecules Sensing Mechanism on Bi and Sn-Doped ZnO Tetrapods

2.8.1. Bi_2O_3-ZnO(0001) Surface

The DFT calculations were performed using plane-wave pseudopotentials[61] and employing the DFT-D2 approach described by Grimme[62] for modeling the interactions of the gas molecules with the surfaces. We have given details about the computation and models employed in the present study in the Computational Details section (Text S1, Supporting Information).

The Zn-terminated polar (0001) surfaces have been found to be the active ZnO surfaces,[63] and as mentioned in the Computational Details section, we started our simulations from our earlier optimized geometry of the reconstructed Zn-terminated ZnO(0001) surface.[64] In this surface structure, each Zn atom is bonded to three oxygen atoms with bond lengths of 1.885 and 1.939 Å in the top surface layer. While modeling the Bi_2O_3:ZnO(0001) surface, different configurations substituting three Zn atoms by two Bi atoms in the first bi-layer were investigated and the most stable configuration was found by replacing two Zn atoms in the top layer by one Bi atom, and one Zn atom in the second layer by another Bi atom. After structural relaxation, the Bi atom in the second layer moves up into the surface to connect via a bond length of 2.666 Å with an O atom in the first layer, which became unsaturated as a result of only one Bi atom replacing two surface Zn atoms. Details of the bond lengths and bonding geometry are shown in Figure S23a (Supporting Information).

We investigated the interaction of an H_2 gas molecule with this Bi_2O_3-ZnO(0001) surface by placing the molecule close to the top surface layer atoms in different initial possible configurations. However, the H_2 molecule moves away from the surface in all the tested configurations, except where it was placed near the surface oxygen atom bonded to the Bi dopants. In this configuration, the H_2 molecule dissociates and forms a surface-bound water molecule that is bound weakly to the Bi atoms, as shown in Figure S23b (Supporting Information). This behavior is similar to the interaction of an H_2 gas molecule on the Zn-doped CuO(111) and Fe-doped ZnO(0001) surfaces, where the H_2 molecule was found to interact with the surface by forming a surface-bound water molecule.[55,64] This interaction of the H_2 molecule with the Bi_2O_3-ZnO(0001) surface releases an energy of 50.04 kJ mol^{-1}.

Similar to the interaction of the H_2 molecule with the surface, the CO molecule interacts with the surface oxygen atom (O_{SUF}) bonded to two Bi atoms. The C atom of the CO molecule connects with the surface oxygen atom (O_{SUF}), while the O atom of the molecule binds to a Bi (Bi1) atom, forming a bent CO_2 molecule as shown in Figure S23c (Supporting Information). As a result of this surface–molecule interaction, a surface oxygen (O_{SUF}) moves up and the Bi(Bi2)-O_{SUF} bond is elongated, with an increase in bond length from 2.199 to 3.344 Å. We note that the CO molecule interacts more strongly with the Bi_2O_3-ZnO(0001) surface than the H_2 molecule, releasing an energy of 173.8 kJ mol^{-1}.

We have plotted the charge density difference between the adsorbed surface–molecule configurations and the bare surface and isolated molecule for both the H_2 and CO molecules (**Figure 9**a,b). As the H_2 molecule forms a surface-bound H_2O

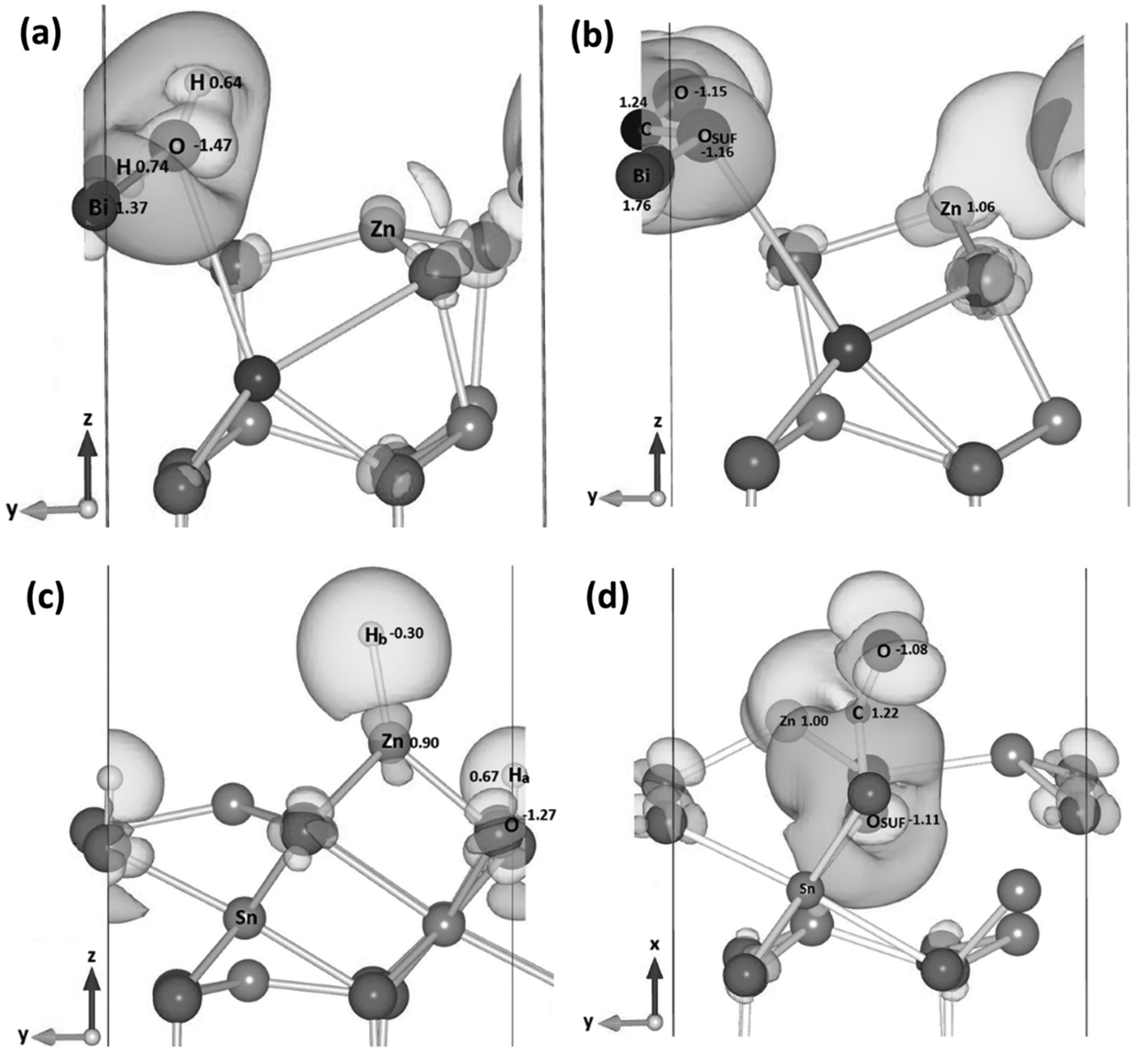

Figure 9. Electronic density difference plot of H_2 and CO bound structures on the a,b) Bi_2O_3-ZnO(0001) surface and c,d) Zn_2SnO_4-ZnO(0001) surface, showing charge transfer in the regions between the molecule and the surface atoms upon interaction. Light gray and dark gray contours indicate electron density increases and decreases, respectively, by 0.004 electrons $Å^{-3}$. Bader charge values are in e^-.

molecule by changing the surface geometry, we note a significant charge transfer, which is also reflected in the change in the Fermi energy, which increases to –0.512 eV from its value of –1.757 eV. Similarly, charge transfer occurs between the CO molecule and the surface, where the molecule gains 0.09 e^- positive charge. Here also, the Fermi energy increases by 0.44 eV, changing its value to –1.319 eV.

2.8.2. Zn_2SnO_4-ZnO(0001) Surface

Similar to the Bi_2O_3-ZnO(0001) surface, we also modeled different configurations of Sn doping by replacing two Zn atoms by one Sn atom in the first bi-layer of the ZnO(0001) surface. The most stable structure is shown in Figure S24a (Supporting Information), where the Sn atom occupies a site at the top of the second layer, leaving the O and Zn atoms more exposed toward the interaction with gas molecules. The Sn dopant atom binds to oxygen atoms in the first layer, which became unsaturated as a result of the Zn vacancy created as a result of the Sn doping. In the relaxed geometry, Sn is found to bind with three oxygen atoms in the top layer and two oxygen atoms below in the second layer. Figure S24a (Supporting Information) shows the detailed bonding arrangement.

For H_2 adsorption, we investigated numerous initial configurations by placing the H_2 molecule close to different surface atoms, including the Sn dopant atom. Upon interaction with the Zn_2SnO_4-ZnO(0001) surfaces, the H_2 molecule dissociates

and one of the H atoms (H_a) binds to a surface O atom ($d_{Ha\text{-}O}$ = 0.975 Å), while the second H atom (H_b) connects with one of the surface Zn atom, with a bond length of 1.533 Å. We note that the Zn atom moves upward to connect with the H_a atom, increasing Zn—O bond lengths to ≈2.28 Å (Figure S24b, Supporting Information). This H_2–surface interaction releases 101.2 kJ mol^{-1} energy, which is almost double the amount of energy released during the H_2 interaction with the Bi_2O_3-ZnO(0001) surface.

The CO molecule interacts with the Zn_2SnO_4-ZnO(0001) surface through its C atom, binding to one of the surface oxygens (O_{SUF}) with a bond length of 1.391 Å, resulting in a bent CO_2 geometry. The O_{SUF} atom moves up, thereby elongating the bond length with the Zn atom in the top layer from 1.994 to 2.591 Å. The other bond lengths are shown in Figure S24c (Supporting Information). We note that the CO molecule binds to the surface exothermally, releasing an energy of –97.2 kJ mol^{-1}, although less strongly than on the Bi_2O_3-ZnO(0001) surface.

The charge density plot and Bader charge analysis show charge transfer between the surface and the H_2 molecule, where the H_a atom loses electrons to become positively charged (0.67 e^-) after binding with the surface oxygen atom, while the H_b atom gains electrons (–0.30 e^-) from the surface Zn atom, which results in a charge redistribution on the surface, as shown in Figure 9b,c. The H_2 molecule thus has split into a proton bound to a surface oxygen, and a hydride ion bound to the surface Zn, similar to H_2 gas molecule dissociation on the Cu_2O(111) surface.[65]

In the case of the interaction of the CO gas molecule with the surface, the molecule loses 0.12 e^- after interacting with the surface oxygen atom. We observed changes in the electronic structure as a result of the interaction of the molecules with the surfaces, as the value of Fermi energy decreases to –2.419 eV in the case of the H_2 gas molecule, while it increases to –1.783 eV after the sorption of the CO gas molecule, from an initial value of –2.220 eV.

3. Conclusions

Hybrid 3D networks and single structures based on ZnO tetrapods (ZnO-T) with Me_xO_y and $Zn_xMe_{1-x}O_y$ (Me = Bi and Sn) with improved gas sensing properties were successfully synthesized in this work. Detailed morphological, structural, vibrational, and optical studies of the materials were performed and discussed. Under the experimental conditions used, the Raman spectra were dominated by the vibrational modes expected for the ZnO wurtzite structure. However, for the hybrid ZnO-T-Zn_2SnO_4 networks additional vibrational modes were identified and assigned to the zinc stannate phase, corroborating the X-ray diffraction patterns. The ZnO-T-Bi_2O_3 hybrid networks demonstrated exellent response and good selectivity for H_2 gas (S_{H2} ≈ 8) at 400 °C operating temperature with p-type sensing behavior. The gas sensing mechanism was explained on the basis of Bi_2O_3–Bi_2O_3 junctions and the modulation of a layer accumulating holes under exposure to the ambient air and the H_2 gas. In the case of ZnO-T-Zn_2SnO_4 hybrid networks, the gas sensing investigations revealed excellent response and sensitivity to CO gas, which was attributed to additionally formed Zn_2SnO_4/ZnO-T heterojunctions, leading to an improvement in resistance modulation of the sensor under exposure to the tested gas. Based on a single structure of ZnO-T-Bi_2O_3 arm and on a single ZnO-T-Zn_2SnO_4 arm or tetrapod, highly selective and ultra-sensitive H_2 gas sensors were obtained that are able to work at room temperature, an important finding for applications with low power consumption. The DFT-based calculations have provided details into the physio-chemical processes of H_2 and CO gas molecule interactions with the Bi- and Sn-doped ZnO(0001) surfaces. The gas molecules interact exothermally with both the surfaces and the electronic structure calculations revealed changes in the Fermi energies as well as the charge transfer between the molecules and surface species. The obtained results are very important for micro- and nanodevice-based sensing applications and in low-power electronics.

4. Experimental Section

Hybrid 3D networks of ZnO-T with Me_xO_y and $Zn_xMe_{1-x}O_y$ (ZnO-T-Me_xO_y and ZnO-T-$Zn_xMe_{1-x}O_y$) were produced by the FTS approach, then ZnO-T networks were mixed with Me (Me = Bi, Sn) microparticles in different weight ratios and subsequently annealed in air in a furnace at 1150 °C for 5 h.[8,22] To synthesize the hybrid networks, the ZnO-T grown by FTS approach were mixed with Bi and Sn metal microparticles, and then were annealed in air. Further details were presented in previous work.[22] SEM, XRD, EDX, micro-Raman measurements were performed as described in a previous work.[8]

The pure and hybrid networked ZnO-T sensor structures were made using a technological flow,[8] and UV and gas sensing measurements were performed as described in earlier reports.[7,8,15–18] The RH value during the measurements was set to 30% RH and 70% RH using a bubbling system, and was measured using a standard hygrometer.[14,17] The UV and gas response was calculated as the ratio of currents in "on" and "off" states (I_{ON}/I_{OFF}) and as the ratio of the currents under exposure to gas and air for n-type (I_{gas}/I_{air}) and p-type (I_{air}/I_{gas}) semiconducting oxides, respectively. The devices based on a single structure were fabricated following the procedure described previously by Lupan et al.[1,18,48,56,66] Details on the DFT calculations are presented in Text S1 (Supporting Information).

Supporting Information

Supporting Information is available from the Wiley Online Library or from the author.

Acknowledgements

O.L. acknowledges the Alexander von Humboldt Foundation for the research fellowship for experienced researchers at the Institute for Materials Science, Kiel University, Germany. The authors acknowledge the support from the German Research Foundation (DFG) under the schemes AD 183/12-1, AD 183/17-1. Additionally, part of the work was funded by FEDER funds through the COMPETE 2020 Programme and FCT (Portuguese Foundation for Science and Technology) funds through the projects UID/CTM/50025/2013 and RECI/FIS-NAN/0183/2012 (FCOMP-01-0124-FEDER-027494). A.K.M. and N.H.d.L. acknowledge the Engineering and Physical Sciences Research Council (EPSRC) "4CU" programme SEED grant (EP/K001329/1 and EP/K035355/1). A.K.M. also acknowledges the startup grant from the University of Petroleum and Energy Studies (UPES), Dehradun, India. N.H.d.L. thanks the Royal Society for an Industry Fellowship. This research was partly supported

by the project Institutional 45inst-15.817.02.29A and by the STCU within the Grant 5989.

Received: September 9, 2016
Revised: October 5, 2016
Published online: December 30, 2016

[1] O. Lupan, L. Chow, G. Chai, *Sens. Actuators, B* **2009**, *141*, 511.
[2] G. Chai, O. Lupan, L. Chow, H. Heinrich, *Sens. Actuators, A* **2009**, *150*, 184.
[3] L. Gan, M. Liao, H. Li, Y. Ma, T. Zhai, *J. Mater. Chem. C* **2015**, *3*, 8300.
[4] G. Y. Chai, L. Chow, O. Lupan, E. Rusu, G. I. Stratan, H. Heinrich, V. V. Ursaki, I. M. Tiginyanu, *Solid State Sci.* **2011**, *13*, 1205.
[5] O. Lupan, L. Chow, T. Pauporté, L. K. Ono, B. Roldan Cuenya, G. Chai, *Sens. Actuators, B* **2012**, *173*, 772.
[6] I. Hölken, G. Neubüser, V. Postica, L. Bumke, O. Lupan, M. Baum, Y. K. Mishra, L. Kienle, R. Adelung, *ACS Appl. Mater. Interfaces* **2016**, *8*, 20491.
[7] D. Gedamu, I. Paulowicz, S. Kaps, O. Lupan, S. Wille, G. Haidarschin, Y. K. Mishra, R. Adelung, *Adv. Mater.* **2014**, *26*, 1541.
[8] Y. K. Mishra, G. Modi, V. Cretu, V. Postica, O. Lupan, T. Reimer, I. Paulowicz, V. Hrkac, W. Benecke, L. Kienle, R. Adelung, *ACS Appl. Mater. Interfaces* **2015**, *7*, 14303.
[9] J.-J. Delaunay, N. Kakoiyama, I. Yamada, *Mater. Chem. Phys.* **2007**, *104*, 141.
[10] D. Calestani, M. Zha, R. Mosca, A. Zappettini, M. C. Carotta, V. Di Natale, L. Zanotti, *Sens. Actuators, B* **2010**, *144*, 472.
[11] L. M. Li, Z. F. Du, T. H. Wang, *Sens. Actuators, B* **2010**, *147*, 165.
[12] Y. Hao, J. Zhao, L. Qin, Q. Guo, X. Feng, P. Wang, *Micro Nano Lett.* **2012**, *7*, 200.
[13] J. Liu, X. Wang, Q. Peng, Y. Li, *Adv. Mater.* **2005**, *17*, 764.
[14] a) D.-J. Yang, I. Kamienchick, D. Y. Youn, A. Rothschild, I.-D. Kim, *Adv. Funct. Mater.* **2010**, *20*, 4258; b) V. Cretu, V. Postica, A. K. Mishra, M. Hoppe, I. Tiginyanu, Y. K. Mishra, L. Chow, N. H. de Leeuw, R. Adelung, O. Lupan, *J. Mater. Chem. A* **2016**, *4*, 6527.
[15] O. Lupan, V. Postica, V. Cretu, N. Wolff, V. Duppel, L. Kienle, R. Adelung, *Phys. Status Solidi RRL* **2016**, *10*, 260.
[16] V. Postica, I. Hölken, V. Schneider, V. Kaidas, O. Polonskyi, V. Cretu, I. Tiginyanu, F. Faupel, R. Adelung, O. Lupan, *Mater. Sci. Semicond. Proc.* **2016**, *49*, 20.
[17] O. Lupan, V. Cretu, V. Postica, O. Polonskyi, N. Ababii, F. Schütt, V. Kaidas, F. Faupel, R. Adelung, *Sens. Actuators, B* **2016**, *230*, 832.
[18] O. Lupan, V. V. Ursaki, G. Chai, L. Chow, G. A. Emelchenko, I. M. Tiginyanu, A. N. Gruzintsev, A. N. Redkin, *Sens. Actuators, B* **2010**, *144*, 56.
[19] a) H.-J. Kim, J.-H. Lee, *Sens. Actuators, B* **2014**, *192*, 607; b) N. Yamazoe, *Sens. Actuators, B* **1991**, *5*, 7.
[20] S. T. Shishiyanu, O. Lupan, E. V. Monaico, V. V. Ursaki, T. S. Shishiyanu, I. M. Tiginyanu, *Thin Solid Films* **2005**, *488*, 15.
[21] a) A. M. Ruiz, G. Sakai, A. Cornet, K. Shimanoe, J. R. Morante, N. Yamazoe, *Sens. Actuators, B* **2003**, *93*, 509; b) Q. Wang, X. Li, F. Liu, Y. Sun, C. Wang, X. Li, P. Sun, J. Lin, G. Lu, *Sens. Actuators, B* **2016**, *230*, 17.
[22] J. Gröttrup, I. Paulowicz, A. Schuchardt, V. Kaidas, S. Kaps, O. Lupan, R. Adelung, Y. K. Mishra, *Ceram. Int.* **2016**, *42*, 8664.
[23] a) N. Van Hieu, N. Duc Chien, *Physica B* **2008**, *403*, 50; b) C. Xiangfeng, J. Dongli, A. B. Djurišic, Y. H. Leung, *Chem. Phys. Lett.* **2005**, *401*, 426.
[24] D. Calestani, R. Mosca, M. Zanichelli, M. Villani, A. Zappettini, *J. Mater. Chem.* **2011**, *21*, 15532.
[25] A. Katoch, Z. U. Abideen, H. W. Kim, S. S. Kim, *ACS Appl. Mater. Interfaces* **2016**, *8*, 2486.
[26] a) Y. K. Mishra, S. Kaps, A. Schuchardt, I. Paulowicz, X. Jin, D. Gedamu, S. Freitag, M. Claus, S. Wille, A. Kovalev, S. N. Gorb, R. Adelung, *Part. Part. Syst. Charact.* **2013**, *30*, 775; b) Y. K. Mishra, S. Kaps, A. Schuchardt, I. Paulowicz, X. Jin, D. Gedamu, S. Wille, O. Lupan, R. Adelung, *KONA Powder Part. J.* **2014**, *31*, 92.
[27] Q. Yuan, Y. P. Zhao, L. Li, T. Wang, *J. Phys. Chem. C* **2009**, *113*, 6107.
[28] a) W. Lisheng, Z. Xiazhong, L. Xing, Y. Weiguo, *Nanotechnology* **2005**, *16*, 2928; b) O. A. Fouad, G. Glaspell, M. S. El-Shall, *Top. Catal.* **2008**, *47*, 84.
[29] K. Jeyadheepan, C. Sanjeeviraja, *J. Chem.* **2014**, *2014*, 245918.
[30] R. Cuscó, E. Alarcón-Lladó, J. Ibáñez, L. Artús, J. Jiménez, B. Wang, M. J. Callahan, *Phys. Rev. B* **2007**, *75*, 165202.
[31] a) R. Loudon, *Adv. Phys.* **1964**, *13*, 423; b) M. Kazan, S. Pereira, M. Correia, P. Masri, *J. Appl. Phys.* **2009**, *106*, 023523.
[32] a) J. Steele, R. Lewis, *Opt. Mater. Express* **2014**, *4*, 2133; b) F. D. Hardcastle, I. E. Wachs, *J. Solid State Chem.* **1992**, *97*, 319.
[33] S. S. Mali, C. S. Shim, C. K. Hong, *Sci. Rep.* **2015**, *5*, 11424.
[34] C. Pang, B. Yan, L. Liao, B. Liu, Z. Zheng, T. Wu, H. Sun, T. Yu, *Nanotechnology* **2010**, *21*, 465706.
[35] X. Shen, J. Shen, S.-J. You, L.-X. Yang, L.-Y. Tang, Y.-C. Li, J. Liu, H. Yang, K. Zhu, Y. Liu, *J. Appl. Phys.* **2009**, *106*, 113523.
[36] O. A. Fouad, G. Glaspell, M. S. El-Shall, *Nano* **2010**, *05*, 185.
[37] a) J. Hou, C. Yang, Z. Wang, W. Zhou, S. Jiao, H. Zhu, *Appl. Catal., B* **2013**, *142*, 504; b) J. Wang, S. Xie, H. Yuan, X. Yan, D. Liu, Y. Gao, Z. Zhou, L. Song, L. Liu, X. Zhao, *Solid State Commun.* **2004**, *131*, 435.
[38] a) H. Morkoç, Ü. Özgür, *Zinc Oxide: Fundamentals, Materials and Device Technology*, Wiley-VCH, Weinheim, Germany **2009**; b) F. Leiter, H. Alves, D. Pfisterer, N. Romanov, D. Hofmann, B. Meyer, *Physica B* **2003**, *340*, 201; c) E. M. Likovich, R. Jaramillo, K. J. Russell, S. Ramanathan, V. Narayanamurti, *Appl. Phys. Lett.* **2011**, *99*, 151910.
[39] A. Janotti, C. G. Van de Walle, *Phys. Rev. B* **2007**, *76*, 165202.
[40] a) A. K. Das, P. Misra, R. Kumar, T. Ganguli, M. Singh, D. Phase, L. Kukreja, *Appl. Phys. A* **2014**, *114*, 1119; b) Y. Dong, F. Tuomisto, B. Svensson, A. Y. Kuznetsov, L. J. Brillson, *Phys. Rev. B* **2010**, *81*, 081201.
[41] R. Dingle, *Phys. Rev. Lett.* **1969**, *23*, 579.
[42] a) T. Nobis, E. M. Kaidashev, A. Rahm, M. Lorenz, M. Grundmann, *Phys. Rev. Lett.* **2004**, *93*, 103903; b) T. Reimer, I. Paulowicz, R. Röder, S. Kaps, O. Lupan, S. Chemnitz, W. Benecke, C. Ronning, R. Adelung, Y. K. Mishra, *ACS Appl. Mater. Interfaces* **2014**, *6*, 7806.
[43] J. Rodrigues, T. Holz, R. F. Allah, D. Gonzalez, T. Ben, M. R. Correia, T. Monteiro, F. M. Costa, *Sci. Rep.* **2015**, *5*, 10783.
[44] G. Sberveglieri, S. Groppelli, P. Nelli, A. Camanzi, *Sens. Actuators, B* **1991**, *3*, 183.
[45] S.-W. Choi, A. Katoch, G.-J. Sun, S. S. Kim, *Sens. Actuators, B* **2013**, *181*, 787.
[46] J. H. Yu, G. M. Choi, *J. Electroceram.* **2002**, *8*, 249.
[47] J. H. Yu, G. M. Choi, *Sens. Actuators, B* **1998**, *52*, 251.
[48] O. Lupan, G. Chai, L. Chow, *Microelectron. Eng.* **2008**, *85*, 2220.
[49] G. Xinglong, L. Rong, W. Guoxiu, C. Zhixin, W. David, *Nanotechnology* **2009**, *20*, 495501.
[50] A. Katoch, J.-H. Kim, Y. J. Kwon, H. W. Kim, S. S. Kim, *ACS Appl. Mater. Interfaces* **2015**, *7*, 11351.
[51] W. J. Moon, J. H. Yu, G. M. Choi, *Sens. Actuators, B* **2002**, *87*, 464.
[52] S. Vetter, S. Haffer, T. Wagner, M. Tiemann, *Sens. Actuators, B* **2015**, *206*, 133.
[53] A. A. Tomchenko, *Sens. Actuators, B* **2000**, *68*, 48.
[54] H.-R. Kim, A. Haensch, I.-D. Kim, N. Barsan, U. Weimar, J.-H. Lee, *Adv. Funct. Mater.* **2011**, *21*, 4456.

[55] O. Lupan, V. Postica, M. Mecklenburg, Y. K. Mishra, K. Schulte, B. Fiedler, R. Adelung, *J. Mater. Chem. A* **2016**, *4*, 16723.
[56] O. Lupan, V. Cretu, V. Postica, M. Ahmadi, B. R. Cuenya, L. Chow, I. Tiginyanu, B. Viana, T. Pauporte, R. Adelung, *Sens. Actuators, B* **2016**, *223*, 893.
[57] a) J. H. Kim, A. Katoch, S. S. Kim, *Sens. Actuators, B* **2016**, *222*, 249; b) C. M. Chang, M. H. Hon, C. Leu, *RSC Adv.* **2012**, *2*, 2469.
[58] J. X. Wang, X. W. Sun, Y. Yang, K. K. A. Kyaw, X. Y. Huang, J. Z. Yin, J. Wei, H. V. Demir, *Nanotechnology* **2011**, *22*, 325704.
[59] J. H. Yu, G. M. Choi, *Sens. Actuators, B* **2001**, *72*, 141.
[60] a) S. N. Das, J. P. Kar, J. H. Choi, T. I. Lee, K. J. Moon, J. M. Myoung, *J. Phys. Chem. C* **2010**, *114*, 1689; b) J. Schalwig, G. Müller, U. Karrer, M. Eickhoff, O. Ambacher, M. Stutzmann, L. Görgens, G. Dollinger, *Appl. Phys. Lett.* **2002**, *80*, 1222; c) M. Shafiei, J. Yu, R. Arsat, K. Kalantar-Zadeh, E. Comini, M. Ferroni, G. Sberveglieri, W. Wlodarski, *Sens. Actuators, B* **2010**, *146*, 507.
[61] a) G. Kresse, J. Furthmüller, *Phys. Rev. B* **1996**, *54*, 11169; b) G. Kresse, J. Furthmüller, *Computer Mater. Sci.* **1996**, *6*, 15; c) G. Kresse, J. Hafner, *Phys. Rev. B* **1994**, *49*, 14251.
[62] S. Grimme, *J. Comput. Chem.* **2006**, *27*, 1787.
[63] a) A. Kornherr, G. E. Nauer, A. A. Sokol, S. A. French, C. R. A. Catlow, G. Ziffer, *Langmuir* **2006**, *22*, 8036; b) H. J. Monkhorst, J. D. Pack, *Phys. Rev. B* **1976**, *13*, 5188.
[64] O. Lupan, V. Postica, J. Gröttrup, A. K. Mishra, N. H. de Leeuw, J. F. C. Carriera, J. Rodrigues, N. Ben, M. R. Correia, T. Monteiro, V. Cretu, I. Tiginyanu, D. Smazna, Y. K. Mishra, R. Adelung, *ACS Appl. Mater. Interfaces* **2016**, under revision.
[65] A. K. Mishra, N. H. de Leeuw, *J. CO2 Util.* **2016**, *15*, 96.
[66] a) O. Lupan, L. Chow, G. Chai, L. Chernyak, O. Lopatiuk-Tirpak, H. Heinrich, *Phys. Status Solidi A* **2008**, *205*, 2673; b) O. Lupan, V. Postica, N. Ababii, M. Hoppe, V. Cretu, I. Tiginyanu, V. Sontea, Th. Pauporté, B. Viana, R. Adelung, *Microelectron. Eng.* **2016**, *164*, 63.

